Journal of Materials Chemistry C

ROYAL SOCIETY OF CHEMISTRY

PAPER

View Article Online
View Journal

Cite this: DOI: 10.1039/d5tc03975d

A light-emitting and detecting bifunctional device based on the bias-selective redox activity of a polymer

Won Jun Pyo,[a] Soohwan Yoo,[a] Sanghyeok An,[a] Taek Min Kim,[a] Junseo Kim,[a] Sangjun Lee,[a] Yong-Young Noh,[a] Dae Seok Kim,*[b] Sangmin Lee,*[a] Young-Ki Kim*[a] and Dae Sung Chung*[a]

Received 8th November 2025,
Accepted 11th March 2026

DOI: 10.1039/d5tc03975d

rsc.li/materials-c

We propose an approach featuring a bifunctional organic device designed to serve as both a light-emitting electrochemical cell and a photodetector in a unified platform. This device enables controlled light emission and detection by manipulating the bias direction and magnitude, leveraging the selective redox activity induced by the ionic liquid. The two-terminal device operates through two key mechanisms: Under reverse bias, the anions, serving as a p-type dopant, permeate the active layer (P3HT), augmenting the photoconductive gain. Conversely, forward bias causes cations to penetrate the P3HT, inducing an n-doping effect, creating a p–i–n junction similar to light-emitting electrochemical cells (LECs). This bias-dependent redox activity combines the features of a photodetector with exceptional performance: an EQE of 10 000%, alongside LEC with a luminance of 17 cd m^{-2}. The successful creation of a two-way VLC system using reverse- or forward-biased devices demonstrated consistent data transmission and reception.

Introduction

Bifunctional photodetectors, capable of operating as both data transmitters and receivers, are integral to the advancement of energy harvesting displays[1] and light-fidelity (Li-Fi) technologies.[2,3] These devices facilitate real-time, two-way communication by simultaneously transmitting and receiving data. Their dual functionality is poised to revolutionize user–device interface interactions, playing a crucial role in the emerging field of wearable Li-Fi technology, a novel wireless optical communication paradigm.[4,5]

To achieve this dual functionality, traditional approaches involved mechanically integrating separate data transmitters, such as light-emitting diodes (LEDs), and receivers, such as photodetectors, into a system.[6] However, this method requires a more complex fabrication process. Consequently, extensive research has been directed toward developing bifunctional photodetectors that combine the functionalities of LEDs and photodetectors into a unified device platform, instead of integrating disparate components.

The initial research in this domain was reported by Yu *et al.* in 1994, who utilized a polymer-based LED framework.[7] They introduced a device structure of Ca/MEH–PPV/ITO exhibiting 1% external quantum efficiency as a PLED, and 0.045 A W^{-1} responsivity as a photodetector. While organic material-based research on bifunctional devices has not been conducted for over three decades after Yu's work, subsequent investigations predominantly focused on exploring inorganic semiconductor materials. Noteworthy examples include CdS/CdSe/ZnSe nanorods,[1] CdSe/ZnS core–shell quantum dots (QDs),[3] bilayer $MoTe_2$ p–n junctions,[8] InGaN/$Al_{0.1}Ga_{0.9}N$ multiquantum well structures,[9] and hybrid perovskite QDs.[2,10] While progress in bifunctional photodetectors using inorganic semiconductors is promising, the development of such devices based on organic semiconductors remains critical for their seamless integration into Li-Fi systems.

The development of organic semiconductor-based light-emitting/detecting bifunctional devices has faced significant challenges. To integrate light-emitting and detecting functions within a single organic device platform, two seemingly contradictory phenomena should be realized: a mechanism for light emission in the active layer through external charge injection and a mechanism for generating and extracting charge to the external circuit *via* light absorption. Traditional complex organic light-emitting diode (OLED) structures comprising layers for electron injection, electron transport, hole blocking, emission, hole transport, and hole injection have proven inadequate for facilitating efficient charge extraction to the external circuitry.[11–13] Similarly, conventional organic photodiode (OPD)

[a] *Department of Chemical Engineering, Pohang University of Science and Technology (POSTECH), Pohang 37673, Republic of Korea*
[b] *Department of Polymer Engineering, Pukyong National University, Busan 48513, Republic of Korea*

configurations such as p–n or Schottky junctions utilizing dopant-free π-conjugated organic semiconductors are inadequate in terms of their light-emitting capabilities.[14–16] Thus, the successful realization of organic semiconductor-based bifunctional devices hinges on establishing conditions that enable the selective derivation of various operating mechanisms by means of controlled stimuli.

In this study, we present a bifunctional organic device capable of both light emission and detection, utilizing the selective redox activity of the active layer under specific external bias conditions through electrochemical charge compensation. This was achieved by treating the PEDOT:PSS with $[EMIM]^+[OTf]^-$, which dispersed mobile ions throughout the film. These ions demonstrate voltage-dependent mobility, facilitating bias-dependent redox activity upon drift into the active layer.[17,18] The modified PEDOT:PSS film thus assumes a dual role: it functions as an efficient hole transport layer and a bias-selective ion-injection layer. Applying a reverse bias to the bifunctional device (negative bias to the PEDOT:PSS side) causes the anionic $[OTf]^-$ species to permeate the P3HT active layer, enabling p-type doping in the vicinity of the depletion region and enhancing the photoconductive gain of the device.[19,20] In contrast, a forward bias leads to the injection of cations ($[EMIM]^+$) into the P3HT layer, inducing n-type doping near the electrode interface and creating a pseudo-p–i–n junction, similar to light-emitting electrochemical cells (LECs).[21–23] This bias-dependent redox activity caused by electrostatic force of the ionic liquid within a single device offers the distinctive characteristics of both an organic photodetector and an organic LEC, thereby emphasizing its bifunctionality.

Experimental

Materials

P3HT and PEDOT:PSS solution (AI4083) were purchased from Ossila and Heraeus, respectively. $[EMIM]^+[OTf]^-$, PEIE, acetone, isopropyl alcohol, 2-methoxyethanol and 1,2-dichlorobenzene were purchased from Sigma Aldrich. All materials were used without further purification.

Device fabrication

The ITO-patterned glass substrates were cleaned by sequential ultrasonic treatment in a Mucasol solution, deionized water, acetone, and isopropyl alcohol for 20 min each. The cleaned glass substrates were dried using N_2 gas flow, followed by 10 min of oxygen plasma to eliminate any residual organic contaminants and to make the substrate hydrophilic. 1 vol% of [EMIM][OTf] was added to the PEDOT:PSS solution and stirred for 3 h at room temperature, then spin coated at 2500 rpm for 60 s on the pre-cleaned ITO substrates followed by thermal annealing at 120 °C for 10 min to evaporate residual moisture. A P3HT solution was prepared by dissolving in 1,2-dichlorobenzene at a concentration of 40 mg mL^{-1}, and stirred at 80 °C for 24 h. The P3HT solution was spin-coated on the top of the PEDOT:PSS layer at 1000 rpm for 60 s and annealed at 150 °C for 20 min in an N_2-filled glove box. PEIE was diluted in 2-methoxyethanol with a concentration of 0.30–0.50 wt% and stirred for 3 h in room temperature. The PEIE solution was spin coated on the top of the P3HT layer at 1500 rpm for 60 s and annealed at 150 °C for 10 min in an N_2-filled glove box. Then metal electrodes were thermally evaporated onto the active layer under a high vacuum, and the active areas of the fabricated bi-functional devices were 0.09 cm^2.

Photodetector characterization

J–V characteristics and EQE spectra were measured using a Keithley 2450 SourceMeter Unit (SMU) and a 330 W Xe arc lamp with an Oriel Cornerstone 130 1/8 m monochromator. Measurements were controlled with home-made LabView programs. The noise current density spectrum was obtained using a Stanford Research SR830 current pre-amplifier and an Agilent 35670A spectrum analyzer. Capacitance was measured using an Agilent 4284A LCR meter. Measurements were done in an N_2 filled glovebox, without encapsulation.

Light-emitting cell characterization

A Thermo Scientific Evolution 220 UV-vis spectrophotometer was used to obtain the UV-vis absorption spectra. Photoluminescence (PL) spectra were measured using a spectrofluorometer/phosphorimeter (FluoroMax Plus-C-P, HORIBA) with a solid-state laser in continuous wave operation and 150 W ozone free xenon lamp sources. Luminance, EQE, and EL spectra were measured simultaneously using a Keithley 2400 SMU and a commercial measurement system (Photo Research Spectra Scan PR650) in a dark box.

Two-way visual light communication characterization

Two-way VLC was measured by applying a voltage signal to the TX unit by manipulating the SMU and function generator, while the RX signal was measured with a current pre-amplifier and digital oscilloscope (Tektronix 4 series B MSO).

Results and discussion

Strategies and mechanisms of the bifunctional device

Expanding upon our conceptual framework, we designed a device featuring a straightforward bottom-illuminated two-terminal photoconductor (PC) structure. This device consists of an ionic liquid (IL)-treated PEDOT:PSS film functioning dually as a hole-transporting layer and bias-selective ion injection layer. The active layer consists of poly(3-hexylthiophene) (P3HT), a widely acknowledged p-type organic semiconductor extensively used in organic electronics and optoelectronics. Additionally, poly(ethyleneimine) ethoxylated (PEIE) has the capability to enhance selective charge transport and device stability by adjusting band bending through its significant interfacial dipole alignment while avoiding Fermi pinning.[24–26]

In Fig. 1b, the ion distribution within the device is illustrated under reverse and forward biases. Under reverse bias (PC mode), high diffusivity of the anions causes their penetration and accumulation within the P3HT layer,[27,28] especially in

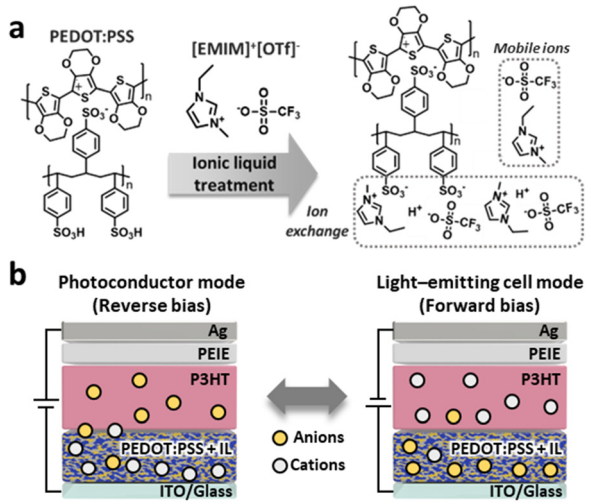

Fig. 1 (a) Schematic of IL-treated PEDOT:PSS. (b) Schematic of the bifunctional device. The ionic distribution within the device is modulated by the external bias.

the vicinity of the P3HT/PEIE interface, leading to an increase in the permittivity of the depletion region.[29] The increase in relative permittivity due to anion penetration potentially reduces the Frenkel exciton binding energy, as demonstrated by the formula:

$$E_b = \frac{q_1 q_2}{4\pi\varepsilon_0\varepsilon_r r}, \quad (1)$$

where ε_0 denotes the vacuum permittivity, ε_r indicates the relative permittivity, q_1 and q_2 represent the elementary charge of holes and electrons, respectively, and r signifies the distance between the holes and electrons. We measured the capacitance of the P3HT film with IL-treated PEDOT:PSS, revealing a significant increase compared to the untreated one (Fig. S1). Despite differences in the experimental conditions for capacitance measurement and device operation, these results substantiate the notion that ion penetration can enhance local permittivity. This enhancement potentially facilitates efficient exciton dissociation within the depletion region, even without a type-II junction or a bulk heterojunction of p- and n-type semiconductors. Such a phenomenon significantly contributes to enhancing the internal quantum efficiency in the photodetectors.[30,31]

Another beneficial aspect of anion penetration into the P3HT layer is its potential for p-doping, which can lead to increased hole mobility.[28,32] Traditional PCs that operate based on a mechanism known as photoconductive gain often achieve an external quantum efficiency (EQE) greater than 100% due to the disparity in charge carrier mobility between majority and minority carriers.[33–35] Recent studies detailing both intrinsic and extrinsic gain generation indicate that the gain of p-type PCs can be mathematically represented by the following equation:[19,20]

$$G = \frac{\tau_r}{\tau_{transit}}\left(1 + \frac{\Delta p}{\Delta n}\frac{\mu_p}{\mu_n}\right), \quad (2)$$

where τ_r denotes the minority carrier recombination lifetime and $\tau_{transit}$ represents the majority carrier transit time. Δp and Δn represent the excess hole and electron densities, respectively, and μ_p and μ_n represent the hole and electron mobilities, respectively. An EQE exceeding 100% is attainable through the generation of gain *via* trapping of minority carriers (electrons in the case of a p-type semiconductor) in localized states within the bandgap of the polymer. This process is facilitated by the accumulation of photogenerated electrons at the interface, enabling multiple hole injections due to current continuity, resulting in a trap-assisted photoconductive gain. Empirical evidence from the IL-treated hole-only device under reverse bias showcased an approximately 15-fold increase in hole mobility within the space charge limited current (SCLC) regime (Fig. S2) compared to the untreated one. This indicates a notable increase in hole carrier density and consequently hole mobility (μ_p), enabled by anion injection into the P3HT film, which induces compensatory hole generation *via* electrochemical doping[29] and thereby further enhances the photoconductive gain of the PC. Conversely, under forward bias in the light-emitting cell mode, the infiltration of cations into the P3HT film, as illustrated in Fig. 1b, resulted in the emission of light. To the best of our knowledge, prior reports on light-emitting devices employing P3HT as an emissive material are absent. This lack of precedent primarily arises because P3HT functions solely as a p-type semiconductor, resulting in an inherent mismatch between hole and electron injection/transport, which are imperative for radiative recombination.[36,37] But why did the P3HT device proposed in this study exhibit bright electroluminescence? Under forward bias conditions, cations accumulated within the P3HT layer, electrostatically compensating for electrons—a process recognized as an electrochemical n-doping of the conjugated polymer.[38,39] This specific process established an "electron pathway" within the P3HT layer. Consequently, it achieved a delicate equilibrium between the hole and electron mobilities within the P3HT layer, while concurrently forming a p–n junction. Within the narrow intrinsic region between the p- and n-type regions, any remaining applied potential dissipated, thereby allowing for radiative electron–hole recombination.[21,22] This mechanism closely resembles the operational principle of a light-emitting electrochemical cell (LEC).[21–23] Hence, we categorize this operational state as the "LEC mode".

Reverse bias: photoconductor mode

In contrast to conventional Schottky diodes with external quantum efficiencies (EQEs) below 100%, the photoconductor developed in this work achieves an EQE exceeding 100% based on a trap-assisted photoconductive mechanism. Upon illumination, the photoconductor accumulates photon-induced electrons at the P3HT/PEIE interface, facilitated by intensified band bending due to the high dipole alignment of the PEIE interlayer[24] (Fig. 2a). Trapped electrons at the interface trigger photomultiplication behavior by reducing the injection barrier for holes from the electrode, akin to the mechanism in photomultiplication-type organic photodiodes (PM-OPDs).[19,40] Additionally, under external bias, enhanced exciton separation by increasing the local permittivity and improved hole mobility through p-doping further amplify the photoconductive gain, as previously discussed.

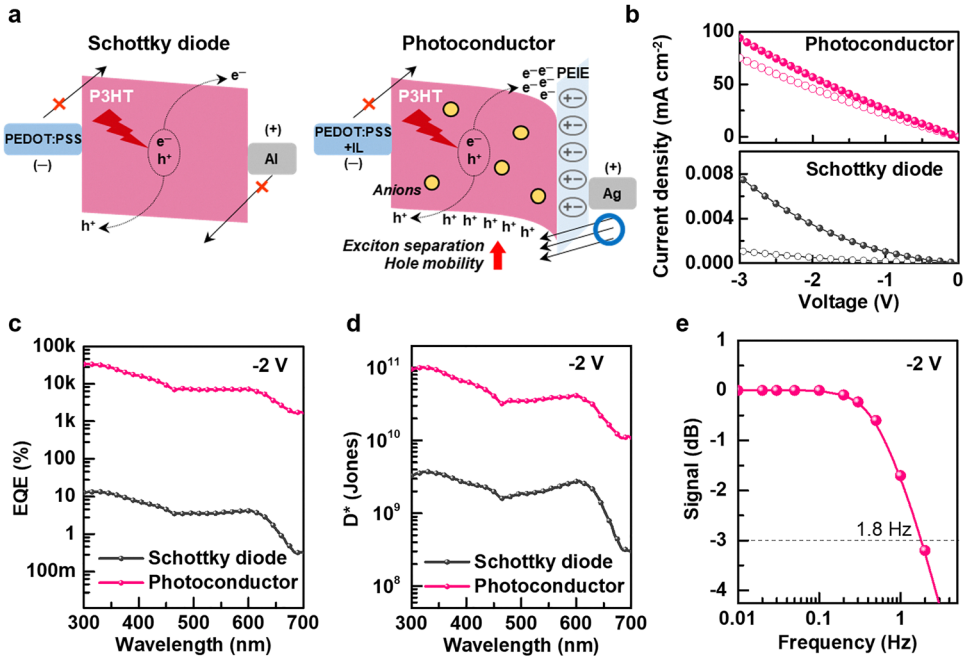

Fig. 2 Photoconductor mode of the bifunctional device under reverse bias. (a) Schematic of the driving mechanism of a conventional Schottky diode (Al/P3HT/PEDOT:PSS/ITO) and the IL-treated photoconductor (Ag/PEIE/P3HT/PEDOT:PSS:IL/ITO). (b) Dark and illuminated (300 nm, 0.12 mW cm^{-2}) *J*–*V* characteristics of the devices. The curve with a filled pattern shows the current density when the light is illuminated. (c) EQE and (d) specific detectivity spectra of the devices measured under −2 V. (e) Bode plot showing cut-off frequency under 300 nm light illumination with an intensity of 0.12 mW cm^{-2}.

The dark and illuminated current density–voltage (*J*–*V*) characteristics of the devices are illustrated in Fig. 2b. The photoconductor exhibited higher dark- and photocurrent compared to the Schottky diode, attributed to enhanced charge injection with trap-assisted photomultiplication and a reduced injection barrier height. To determine the voltage dependence of the photogenerated current, the EQE was calculated using the following equation:

$$\mathrm{EQE} = \frac{hc}{q\lambda}R, \tag{3}$$

where h is Plank's constant, and c denotes the velocity of the light, q indicates the elementary charge, λ denotes the wavelength of the incident light, and R represents current generation (A) per input light power (W). The EQE spectra for the devices are illustrated in Fig. 2c. While the Schottky diode has less than 20% EQE at 300–700 nm wavelength, the PC showed over 7000% EQE in the visible light region. The EQE spectral shape for devices is inversely correlated with the absorption spectra of P3HT where the maximum peak appears near a wavelength of 500 nm, which means that depletion regions for the three devices are formed at the side of the P3HT/metal electrode interface.[41,42]

Specific detectivity (D^*) is a crucial parameter for assessing photodetector performance. It can be calculated using the following equation:

$$D^* = \frac{q\lambda\sqrt{A}\mathrm{EQE}}{hci_{\mathrm{noise}}}, \tag{4}$$

where i_{noise} denotes the noise current (Fig. S3), and A represents the area of the photoactive layer. Based on the EQE spectra and i_{noise}, the peak values of D^* for the Schottky diode and PC were 3.8×10^9, and 1.1×10^{11} Jones, respectively (Fig. 2d). Despite the substantial responsivity enhancement of the IL-treated PC, the increase in specific detectivity was limited by a concurrent rise in i_{noise}. We attribute the increase in i_{noise} primarily to enhanced current fluctuations arising from (i) ionic motion and its temporal fluctuations, (ii) trap-assisted carrier injection/extraction processes, and (iii) interfacial charge accumulation, which modulates charge injection barriers and current pathways. Suppressing these noise sources through materials and device optimization should substantially improve the sensing capability of the device.

Response speed, crucial for integration into visual-light communication systems, was measured in cut-off frequencies (Fig. 2e). The IL-treated PC showed a cut-off frequency of 1.8 Hz; however, the observed cutoff frequency is low compared to state-of-the-art organic photodetectors that exceed 1 MHz.[43,44] This slower response speed is characteristic of the photodetectors that exhibit extrinsic gain through the accumulation of minority carriers, significantly relying on the recombination lifetime of these carriers (eqn (2)). Nonetheless, further enhancements in response speed can be achieved through material and device structure optimization, including tuning the molecular weight of the emissive material, optimizing the concentration/composition of the IL, and interfacial engineering to mitigate recombination-related delays, as seen in previous research on PM-OPDs achieving exceptionally high cutoff frequencies.[45] Although trap-assisted gain enhancement is a well-established mechanism, the more important aspect of our device is its bias-dependent multifunctionality, particularly the

emergence of electroluminescence under forward bias as shown in the following section.

Forward bias: LEC mode

Before exploring the light-emitting properties of the bifunctional device, we initially observed significant modulation in its optical properties following treatment with IL. In Fig. 3a, the absorption and normalized photoluminescence spectra of both IL-treated and untreated devices are depicted. Minimal variation was observed in absorbance, indicating that the presence of ions had a negligible impact on exciton generation. However, the photoluminescence (PL) intensity of the IL-treated device was notably five times higher than that of the untreated one. This discovery suggests that ions diffusing into the P3HT layer exert electrostatic forces, effectively suppressing nonradiative interfacial quenching. Consequently, the IL-treated device demonstrated a higher internal quantum efficiency, signifying an improved capacity to convert absorbed energy into radiative recombination (light) rather than dissipating it through nonradiative processes (heat or vibration).

Fig. 3b illustrates the driving mechanism of the LEC mode under forward bias. As in conventional LECs, ion redistribution can establish a p–i–n junction; in our case, because the active layer is a p-type polymer semiconductor, cation injection into P3HT during forward bias induces a localized p–i–n junction and opens an electron-transport pathway. The cations act as n-dopants in P3HT, enabling junction formation and promoting a delicate balance between hole and electron mobility. This process enables local electron conduction despite P3HT being a p-type material, allowing excitons to undergo radiative recombination rather than being quenched (Fig. 3c). To investigate the light-emitting characteristics under forward bias, we conducted measurements for electroluminescence (EL) spectra, EQE, and luminance, as depicted in Fig. 3d and e. The EL and PL spectra closely overlap in the 600–800 nm range, providing strong evidence that P3HT acts as the emissive material in the device. Consequently, the device emitted intense red light at a peak wavelength of 680 nm in the EL spectra. The luminance reached 17 cd m^{-2} at 8.8 V, with the peak EQE recorded at 0.34%. While these values appear relatively modest compared to OLEDs and LECs documented in previous studies where optimized iridium-based LECs showed EQE over 10%,[11,46] this research marks an initial stride in developing a bifunctional device with traditional organic semiconductors, displaying reasonable detectivity and luminescence. Performance is expected to improve further through enhanced charge balance and reduced nonradiative recombination, particularly interfacial quenching.

It's noteworthy that the high EQE exceeding 10 000% in the photoconductor mode enables self-amplification even under weak light conditions. Consequently, visible-light communication (VLC) can be feasibly achieved through reciprocal communication between identical devices biased in the reverse and forward modes.

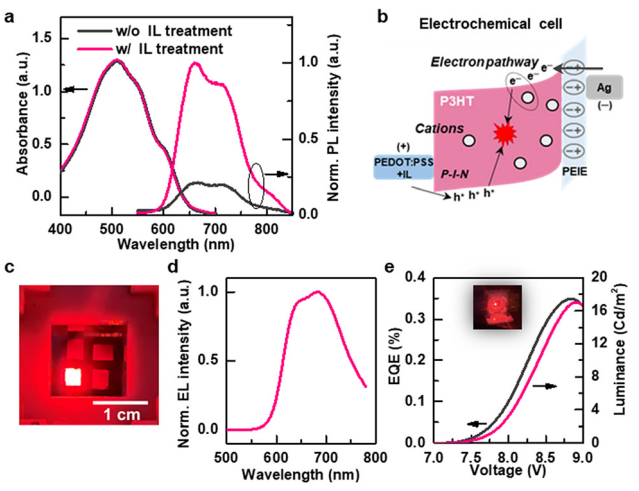

Fig. 3 Optoelectronic characteristics of the bifunctional device. (a) Absorption and normalized photoluminescence (PL) spectra of untreated and IL-treated devices. The sample was fabricated with the structure of P3HT/PEDOT:PSS:IL/Glass. λ_{ex} was 450 nm for PL spectra measurement. (b) Schematic of the driving mechanism for the LEC mode of the bifunctional device. (c) Image of the LEC mode of the device captured by a digital camera. (d) Electroluminescence spectra of the device. (e) EQE and luminance of the bifunctional device.

Two-way visual-light communication using bifunctional devices

A two-way VLC between a reverse-biased device (PC) and a forward-biased device (LEC) was established using bifunctional devices, each with an area of 0.3 cm × 0.3 cm mounted on a 2.5 cm × 2.5 cm glass slide module, as depicted in Fig. 4a. Fig. 4b and c show the waveforms transmitted and received through the two-way VLC system. The wave frequency, initiated by a function generator, operated at approximately 0.1 Hz, with the forward-biased device (LEC) positioned 5 mm away from the reverse-biased device (PC). Despite the presence of minor

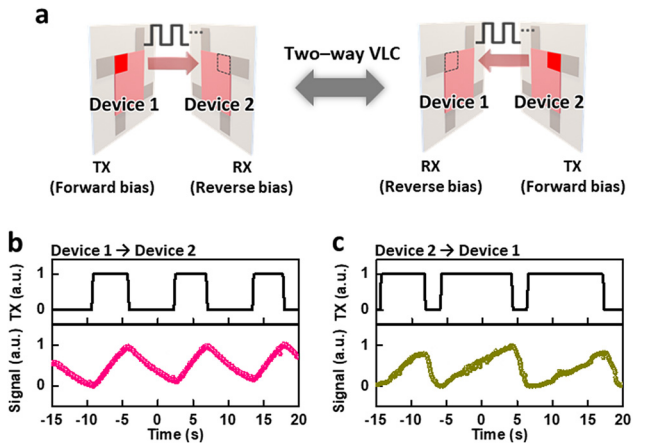

Fig. 4 Demonstration of a two-way visible-light communication system with bifunctional devices. (a) Schematic of two-way communication based on identical bifunctional devices. A random square-wave pattern of a magnitude of 10 V was applied to the transmitter unit (TX) and −0.5 V of bias was applied to the receiver unit (RX). (b) and (c) TX and the received signal when transmitting data from Device 1 to Device 2 and from Device 2 to Device 1, respectively.

crosstalk or noise in the received waveforms, a strong correspondence between the transmitted and received data patterns was clear. Although the EQE decreased by approximately 50% after 20 TX-to-RX transitions (Fig. S4), primarily due to hysteresis and degradation arising from continuous ionic drift, these experimental results nevertheless provide a proof-of-concept demonstration of the practicality and viability of this integrated platform for two-way VLC applications.

Conclusion

To date, VLC systems have relied primarily on one-way data transmission. Expanding these systems to accommodate mutual data transmission holds immense potential, opening doors for two-way VLC systems to flourish. Such a bidirectional communication system requires a single-device platform that can adeptly perform both data transmission and reception functions simultaneously. However, achieving this bifunctionality in devices based on organic semiconductors has remained a challenge. In this study, we achieved the dual functionalities of a data transmitter and receiver in a singular device platform by introducing the bias-selective redox activity induced by the ionic liquid. Specifically, we engineered the functionality of a light-emitting electrochemical cell by introducing cations (n-dopants) into the P3HT layer under forward bias, while simultaneously enabling the functionality of a photoconductor through the infiltration of anions (p-dopants) under reverse bias. Furthermore, we showcased the practicality of two-way optical communication utilizing a singular device platform with inherent bifunctionality. With ongoing enhancements aimed at refining the light-emitting and light-detecting capabilities of these bifunctional organic devices, alongside their integration into flexible, stretchable platforms, we hold an optimistic outlook for the development of a truly wearable two-way VLC product.

Author contributions

W. J. P. carried out most of the experimental work and data analyses. S. Y., S. A., T. M. K., J. K., S. L. and Y.-Y. N. assisted with data curation. D. S. K., S. L., Y.-K. K., and D. S. C. supervised the work. All authors have contributed to the interpretation of the results and the preparation of the manuscript, which was drafted by W. J. P.

Conflicts of interest

The authors declare no competing interests.

Data availability

The experimental data that support the findings of this study are available from the corresponding author upon reasonable request.

Supplementary information (SI) is available. See DOI: https://doi.org/10.1039/d5tc03975d.

Acknowledgements

This research was supported by the National R&D Program through the National Research Foundation of Korea (NRF) funded by the Ministry of Science and ICT (RS-2024-00411809).

Notes and references

1 N. Oh, B. H. Kim, S.-Y. Cho, S. Nam, S. P. Rogers, Y. Jiang, J. C. Flanagan, Y. Zhai, J.-H. Kim, J. Lee, Y. Yu, Y. K. Cho, G. Hur, J. Zhang, P. Trefonas, J. A. Rogers and M. Shim, *Science*, 2017, **355**, 616–619.
2 Q. Shan, C. Wei, Y. Jiang, J. Song, Y. Zou, L. Xu, T. Fang, T. Wang, Y. Dong, J. Liu, B. Han, F. Zhang, J. Chen, Y. Wang and H. Zeng, *Light: Sci. Appl.*, 2020, **9**, 163.
3 T. Y. Kim, S. Park, B. J. Kim, S. B. Heo, J. H. Yu, J. S. Shin, J.-A. Hong, B.-S. Kim, Y. D. Kim, Y. Park and S. J. Kang, *Sci. Rep.*, 2021, **11**, 1700.
4 S. Li, A. Pandharipande and F. M. J. Willems, *IEEE Trans. Commun.*, 2017, **65**, 740–750.
5 P. H. Pathak, X. Feng, P. Hu and P. Mohapatra, *IEEE Commun. Surv. Tutorials*, 2015, **17**, 2047–2077.
6 T. Chiba, D. Kumagai, K. Udagawa, Y. Watanabe and J. Kido, *Sci. Rep.*, 2018, **8**, 11472.
7 G. Yu, C. Zhang and A. J. Heeger, *Appl. Phys. Lett.*, 1994, **64**, 1540–1542.
8 Y.-Q. Bie, G. Grosso, M. Heuck, M. M. Furchi, Y. Cao, J. Zheng, D. Bunandar, E. Navarro-Moratalla, L. Zhou, D. K. Efetov, T. Taniguchi, K. Watanabe, J. Kong, D. Englund and P. Jarillo-Herrero, *Nat. Nanotechnol.*, 2017, **12**, 1124–1129.
9 L. W. Ji, S. J. Young, C. H. Liu, W. Water, T. H. Meen and W. Y. Jywe, *J. Cryst. Growth*, 2008, **310**, 2476–2479.
10 N. Li, Y. S. Lau, Y. Miao and F. Zhu, *Nanophotonics*, 2018, **7**, 1981–1988.
11 S.-J. Zou, Y. Shen, F.-M. Xie, J.-D. Chen, Y.-Q. Li and J.-X. Tang, *Mater. Chem. Front.*, 2020, **4**, 788–820.
12 A. Salehi, X. Fu, D.-H. Shin and F. So, *Adv. Funct. Mater.*, 2019, **29**, 1808803.
13 S. Negi, P. Mittal and B. Kumar, *Microsyst. Technol.*, 2018, **24**, 4981–4989.
14 R. D. Jansen-van Vuuren, A. Armin, A. K. Pandey, P. L. Burn and P. Meredith, *Adv. Mater.*, 2016, **28**, 4766–4802.
15 S. Ying, Z. Ma, Z. Zhou, R. Tao, K. Yan, M. Xin, Y. Li, L. Pan and Y. Shi, *IEEE Access*, 2020, **8**, 189646–189660.
16 J. Liu, M. Gao, J. Kim, Z. Zhou, D. S. Chung, H. Yin and L. Ye, *Mater. Today*, 2021, **51**, 475–503.
17 A. Marks, S. Griggs, N. Gasparini and M. Moser, *Adv. Mater. Interfaces*, 2022, **9**, 2102039.
18 J. O. Guardado and A. Salleo, *Adv. Funct. Mater.*, 2017, **27**, 1701791.

19 J. Kim, M. Kang, S. Lee, C. So and D. S. Chung, *Adv. Mater.*, 2021, **33**, 2104689.
20 Y. Dan, X. Zhao, K. Chen and A. Mesli, *ACS Photonics*, 2018, **5**, 4111–4116.
21 S. van Reenen, P. Matyba, A. Dzwilewski, R. A. J. Janssen, L. Edman and M. Kemerink, *J. Am. Chem. Soc.*, 2010, **132**, 13776–13781.
22 G. G. Malliaras, J. D. Slinker, J. A. DeFranco, M. J. Jaquith, W. R. Silveira, Y.-W. Zhong, J. M. Moran-Mirabal, H. G. Craighead, H. D. Abruña and J. A. Marohn, *Nat. Mater.*, 2008, **7**, 168.
23 Y. Shao, G. C. Bazan and A. J. Heeger, *Adv. Mater.*, 2007, **19**, 365–370.
24 Q. Chen, C. Wang, Y. Li and L. Chen, *J. Am. Chem. Soc.*, 2020, **142**, 18281–18292.
25 H. Ishii, K. Sugiyama, E. Ito and K. Seki, *Adv. Mater.*, 1999, **11**, 605–625.
26 B. A. E. Courtright and S. A. Jenekhe, *ACS Appl. Mater. Interfaces*, 2015, **7**, 26167–26175.
27 E. Zeglio and O. Inganäs, *Adv. Mater.*, 2018, **30**, 1800941.
28 J. Rivnay, S. Inal, A. Salleo, R. M. Owens, M. Berggren and G. G. Malliaras, *Nat. Rev. Mater.*, 2018, **3**, 17086.
29 D. Tsokkou, P. Cavassin, G. Rebetez and N. Banerji, *Mater. Horiz.*, 2022, **9**, 482–491.
30 Z. Wu, Y. Zhai, W. Yao, N. Eedugurala, S. Zhang, L. Huang, X. Gu, J. D. Azoulay and T. N. Ng, *Adv. Funct. Mater.*, 2018, **28**, 1805738.
31 J. Brebels, J. V. Manca, L. Lutsen, D. Vanderzande and W. Maes, *J. Mater. Chem. A*, 2017, **5**, 24037–24050.
32 B. D. Paulsen and C. D. Frisbie, *J. Phys. Chem. C*, 2012, **116**, 3132–3141.
33 J. Miao and F. Zhang, *Laser Photonics Rev.*, 2019, **13**, 1800204.
34 W. Wang, F. Zhang, M. Du, L. Li, M. Zhang, K. Wang, Y. Wang, B. Hu, Y. Fang and J. Huang, *Nano Lett.*, 2017, **17**, 1995–2002.
35 J. Kim, H. Kweon, M. Lee, M. Kang, S. Lee, S. An, W. Lee, S. Choi, H. Choi, Y. Seong, H. Ham, H. Cha, J. Lim, D. H. Kim, B. Kim and D. S. Chung, *Adv. Mater.*, 2023, **35**, 2302786.
36 M. Kuik, G.-J. A. H. Wetzelaer, H. T. Nicolai, N. I. Craciun, D. M. De Leeuw and P. W. M. Blom, *Adv. Mater.*, 2014, **26**, 512–531.
37 S. L. M. van Mensfoort, J. Billen, M. Carvelli, S. I. E. Vulto, R. A. J. Janssen and R. Coehoorn, *J. Appl. Phys.*, 2011, **109**, 064502.
38 Y. Lei, P. Li, Y. Zheng and T. Lei, *Mater. Chem. Front.*, 2024, **8**, 133–158.
39 D. Ohayon, A. Savva, W. Du, B. D. Paulsen, I. Uguz, R. S. Ashraf, J. Rivnay, I. McCulloch and S. Inal, *ACS Appl. Mater. Interfaces*, 2021, **13**, 4253–4266.
40 L. Shi, Q. Liang, W. Wang, Y. Zhang, G. Li, T. Ji, Y. Hao and Y. Cui, *Nanomaterials*, 2018, **8**, 713.
41 A. Armin, R. D. Jansen-van Vuuren, N. Kopidakis, P. L. Burn and P. Meredith, *Nat. Commun.*, 2015, **6**, 6343.
42 A. Yazmaciyan, P. Meredith and A. Armin, *Adv. Opt. Mater.*, 2019, **7**, 1801543.
43 N. Strobel, N. Droseros, W. Köntges, M. Seiberlich, M. Pietsch, S. Schlisske, F. Lindheimer, R. R. Schröder, U. Lemmer, M. Pfannmöller, N. Banerji and G. Hernandez-Sosa, *Adv. Mater.*, 2020, **32**, 1908258.
44 J. Zheng, D. Yang, D. Guo, L. Yang, J. Li and D. Ma, *ACS Photonics*, 2023, **10**, 1382–1388.
45 S. G. Han, H. Lee, W. Choi, D. Lee, S. Kim, Y. Sung, S. Kim and K. Cho, *Adv. Funct. Mater.*, 2021, **31**, 2102087.
46 S. B. Meier, D. Tordera, A. Pertegás, C. Roldán-Carmona, E. Ortí and H. J. Bolink, *Mater. Today*, 2014, **17**, 217–223.